

See discussions, stats, and author profiles for this publication at: <https://www.researchgate.net/publication/255705988>

A visual motion detection circuit suggested by Drosophila connectomics

Article in *Nature* · August 2013

DOI: 10.1038/nature12450 · Source: PubMed

CITATIONS

529

READS

534

24 authors, including:



Shin-ya Takemura

Howard Hughes Medical Institute

36 PUBLICATIONS 2,430 CITATIONS

[SEE PROFILE](#)



Zhiyuan Lu

Dalhousie University

41 PUBLICATIONS 2,558 CITATIONS

[SEE PROFILE](#)



William T Katz

Janelia Farm Research Campus

28 PUBLICATIONS 1,340 CITATIONS

[SEE PROFILE](#)



Ting Zhao

Howard Hughes Medical Institute

51 PUBLICATIONS 2,279 CITATIONS

[SEE PROFILE](#)

Some of the authors of this publication are also working on these related projects:



Reconstruct wiring diagrams of the fly brain [View project](#)



DVID: Distributed Versioned Image-oriented Dataservice [View project](#)

A visual motion detection circuit suggested by *Drosophila* connectomics

Shin-ya Takemura¹, Arjun Bharioke¹, Zhiyuan Lu^{1,2}, Aljoscha Nern¹, Shiv Vitaladevuni¹, Patricia K. Rivlin¹, William T. Katz¹, Donald J. Olbris¹, Stephen M. Plaza¹, Philip Winston¹, Ting Zhao¹, Jane Anne Horne², Richard D. Fetter¹, Satoko Takemura¹, Katerina Blazek¹, Lei-Ann Chang¹, Omotara Ogundeyi¹, Mathew A. Saunders¹, Victor Shapiro¹, Christopher Sigmund¹, Gerald M. Rubin¹, Louis K. Scheffer¹, Ian A. Meinertzhagen^{1,2} & Dmitri B. Chklovskii¹

Animal behaviour arises from computations in neuronal circuits, but our understanding of these computations has been frustrated by the lack of detailed synaptic connection maps, or connectomes. For example, despite intensive investigations over half a century, the neuronal implementation of local motion detection in the insect visual system remains elusive. Here we develop a semi-automated pipeline using electron microscopy to reconstruct a connectome, containing 379 neurons and 8,637 chemical synaptic contacts, within the *Drosophila* optic medulla. By matching reconstructed neurons to examples from light microscopy, we assigned neurons to cell types and assembled a connectome of the repeating module of the medulla. Within this module, we identified cell types constituting a motion detection circuit, and showed that the connections onto individual motion-sensitive neurons in this circuit were consistent with their direction selectivity. Our results identify cellular targets for future functional investigations, and demonstrate that connectomes can provide key insights into neuronal computations.

Vision in insects has been subject to intense behavioural¹, physiological² and anatomical³ investigations, yet our understanding of its underlying neural computations is still far from complete. One such computation, ethologically highly relevant, is motion detection, which is thought to rely on the comparison between signals offset in space and time^{4–6} (Fig. 1a, b). Yet, despite being the focus of theoretical and experimental investigations for more than half a century⁷, the exact mechanism underlying this computation remains a mystery. A central impediment towards unravelling this mechanism has been our incomplete knowledge of the relevant neurons and synapses.

In the fly, visual processing begins in the optic lobe, composed of four retinotopically organized neuropils. Each is an array of repeating modules corresponding to the hexagonal lattice of ommatidia in the compound eye (Fig. 1c). Each module of the first neuropil, the lamina, contains a repeating circuit^{8,9} receiving inputs from six photoreceptors detecting light from the same location in the visual field. The output cells of each lamina module project to a corresponding module of the second neuropil, the medulla (Fig. 1c). Each medulla module, called a column (Fig. 1d), is also thought to contain stereotypic circuits¹⁰. These columns, in turn, innervate two downstream neuropils, the lobula and lobula plate (Fig. 1c).

Responses to local motion must be computed at least partly within the stereotypical circuits of the medulla columns. Indeed, the medulla is the first neuropil with movement-specific activity¹¹, and, directly downstream of the medulla, lobula plate tangential cells (LPTCs) integrate local motion signals to produce wide-field motion response^{12,13}. However, up until now, the lack of a medulla connectome has frustrated investigations of local motion detection.

Semi-automated connectome reconstruction

To provide a reliable foundation for computational modelling and identify targets for electro/optophysiological recordings, we attempted a complete, dense reconstruction of the chemical synaptic connectivity within the medulla using electron microscopy, the gold standard of

neuroanatomy¹⁴. Given the time-consuming nature of such reconstructions, we wanted to determine the smallest medulla volume, reconstruction of which would allow us to identify a circuit underlying the computation of local motion. Both directional turning responses¹⁵ and electrophysiological responses in LPTCs¹⁶ can be elicited in flies by sequential stimulation of two photoreceptors corresponding to adjacent points anywhere in the visual field¹⁷. This suggests that some repeating component of the motion detecting circuit must be present within any two adjacent medulla columns. We therefore decided to reconstruct all the synaptic connections among neurons within a single reference column, as well as all the connections between the reference column and neurons within six nearest-neighbour columns (Fig. 1d).

Because manual reconstruction of even a seven-column volume would be prohibitively time-consuming¹⁸, we developed a semi-automated reconstruction pipeline¹⁹ and applied it to the medulla volume (Fig. 2, Methods and Supplementary Data 1), reconstructing 379 cells (Supplementary Fig. 1 and Supplementary Video 1).

To map our reconstruction onto the existing body of knowledge, we assigned these cells to previously proposed cell types²⁰ by comparing the shapes of reconstructed arbors (Supplementary Fig. 1) with those reported from light microscopy using Golgi impregnation or genetic single-cell labelling (Fig. 2e, f and Supplementary Methods). Because there were several reconstructed examples for almost all neuronal types (Supplementary Fig. 1 and Supplementary Table 2), it was possible to characterize the common structural features of each type. In many cases, this allowed us to match unequivocally a reconstructed cell with a Golgi impregnate²⁰, for which it was then named (Supplementary Methods). However, there was also a subset of cell types for which a Golgi counterpart could not be found but which we validated using isomorphs from genetic single-cell labelling. We named these cell types Mi13, Mi14, Mi15, TmY14, Dm9, and Dm10 (Supplementary Fig. 2). In total, from the collection of 379 reconstructed cells (Supplementary Fig. 1) we were able to classify 290 of them into 56 cell types (Supplementary Table 2).

¹Janelia Farm Research Campus, HHMI, Ashburn, Virginia 20147, USA. ²Department of Psychology and Neuroscience, Dalhousie University, Halifax, Nova Scotia B3H 4R2, Canada.

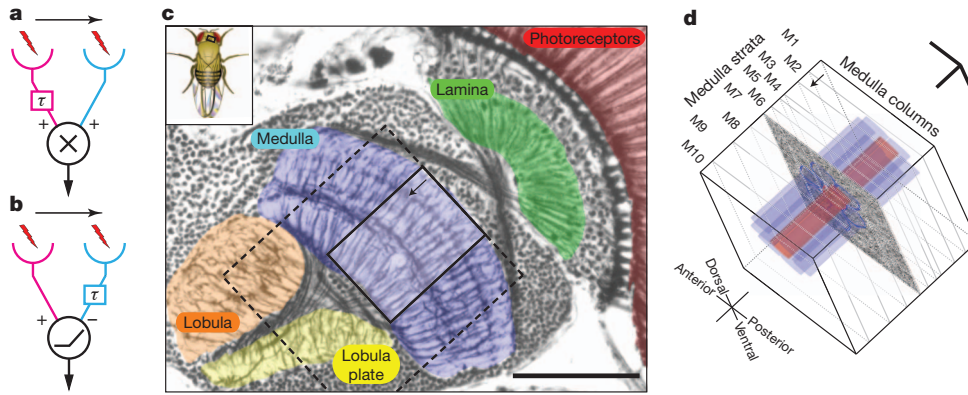


Figure 1 | Motion detection and the *Drosophila* visual system. **a**, Rightward motion component of the Hassenstein–Reichardt EMD⁴ model. Light input (lightning bolt) into the left channel (magenta) is transmitted with an additional delay, τ , relative to that into the right channel (cyan). For a rightwards-moving object, signals from both channels will arrive at the multiplication unit closer in time to each other, and therefore become nonlinearly enhanced (and vice versa for leftwards-moving objects). As a result, the model responds preferentially to rightward motion. **b**, Alternative Barlow–Levick-like EMD⁶ model, also preferring rightward motion. Note that the

inputs are combined with opposing signs and the delay is now in the right (cyan) channel. **c**, Bodian silver-stained horizontal section⁴⁵ of the *Drosophila melanogaster* visual system revealing the four neuropils of the optic lobe. The medulla region of interest (solid rectangle, expanded in **d**) and the wider imaged volume (dashed rectangle) used to trace into the lobula plate are shown schematically. **d**, The $37\ \mu\text{m} \times 37\ \mu\text{m}$ medulla region of interest is centred on the reference column (red) and six surrounding nearest-neighbour columns (blue). The medulla has ten strata (M1–M10) defined by the arborizations of its cell types. Scale bars, $50\ \mu\text{m}$ (**c**) and $10\ \mu\text{m}$ (**d**, in all three directions).

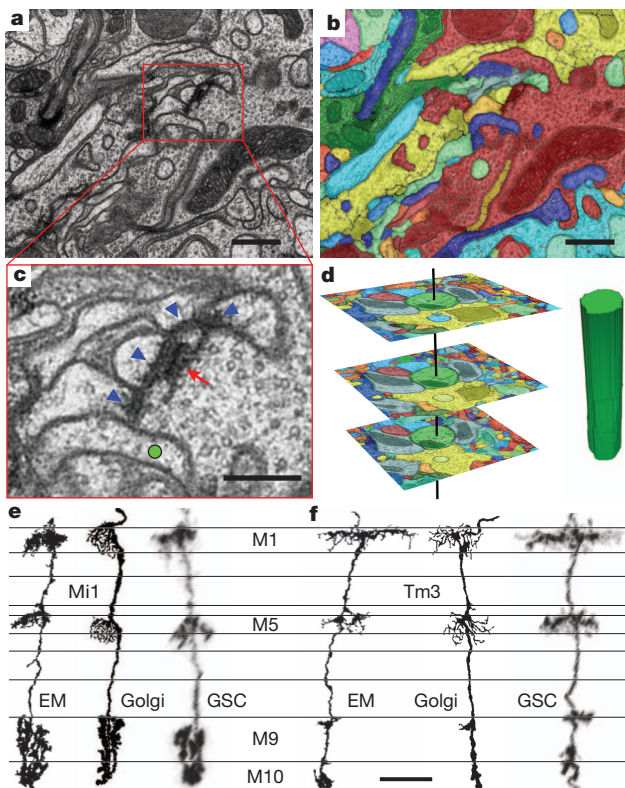


Figure 2 | Connectome reconstruction using serial-section electron microscopy. **a**, A representative micrograph, one of 2,769 from the electron microscopy series. **b**, Proofread segmentation of the micrograph in **a** into neurite profiles (single colours). **c**, Synapses comprise a presynaptic process containing a T-bar ribbon (red arrow) and associated neurites with postsynaptic densities (PSDs) (blue arrowheads) adjacent to the T-bar. A non-synaptic process (green circle) lacks a PSD (in both this and other section planes containing this T-bar). **d**, Neurites are reconstructed by linking profiles in consecutive sections (left), to construct a 3D object (right). **e**, An example of a neuron reconstructed from electron microscopy (left), identified by comparison with the Golgi impregnated cell (centre)²⁰ as type Mi1 and cross-validated by a corresponding genetic single-cell (GSC)-labelled neuron (right) (Supplementary Methods). **f**, Same as **e** for cell type Tm3. Scale bars, $500\ \text{nm}$ (**a**, **b**), $250\ \text{nm}$ (**c**) and $10\ \mu\text{m}$ (**e**, **f**).

To reveal the connections between the 379 reconstructed neurons, we identified pre- and postsynaptic sites and assigned them to their respective parent cells. Within the reference column and its immediate surround, we annotated 10,093 presynaptic sites and 38,465 associated postsynaptic sites (3.8 ± 1.2 (mean \pm s.d.) per presynaptic site) (Fig. 2c and Supplementary Table 1). Although presynaptic T-bars typically fell onto proofread profiles of neurons, postsynaptic sites usually fell onto isolated profiles, unassigned to any neuron. Thus, it was necessary to trace the dendrite containing each postsynaptic site back to a parent cell. This postsynaptic tracing was extremely challenging as *Drosophila* neuron dendrites branch elaborately and, indeed, can be thinner than the section thickness.

The challenging postsynaptic tracing led to (1) some erroneously identified synaptic contacts, and (2) a high fraction ($\sim 50\%$) of contacts that could not be traced to their parent neuron and were therefore unidentified. To increase our confidence in the identified contacts (1), we had two proofreaders trace every postsynaptic site (Methods), and only accepted into the connectome those contacts that both proofreaders identified independently. By contrast, it was not possible to reduce the number of unidentified contacts experimentally (2). However, we were still able to construct a connectome valuable for inferring function because we found that, within the medulla, connections of high weight (that is, high number of synaptic contacts per connection) both capture a large fraction of the total connection weight and can be identified with high fidelity. Indeed, the distribution of connection weight in our connectome is heavy tailed (Fig. 3b, inset, and Supplementary Fig. 3), as has been found in other organisms^{21,22}. Also, assuming that synapses are equally difficult to proofread, we found that any strong connection (with >5 synaptic contacts) will be identified with $>95\%$ probability. Therefore, in the resulting connectome, 8,637 synaptic contacts are precisely identified, and all strong connections are represented.

The connectome module and its pathways

To identify pathways performing local computations such as motion detection, it was necessary to generate a more convenient abstraction of the full connectome. Because we expect that the circuits of interest repeat within each column, we extracted from the medulla connectome a periodic module of connections between identified cell types that arborize in every column. These include both so-called synperiodic cell types with single neurons in every column of the medulla²³, and cell types with several members within each column, which we

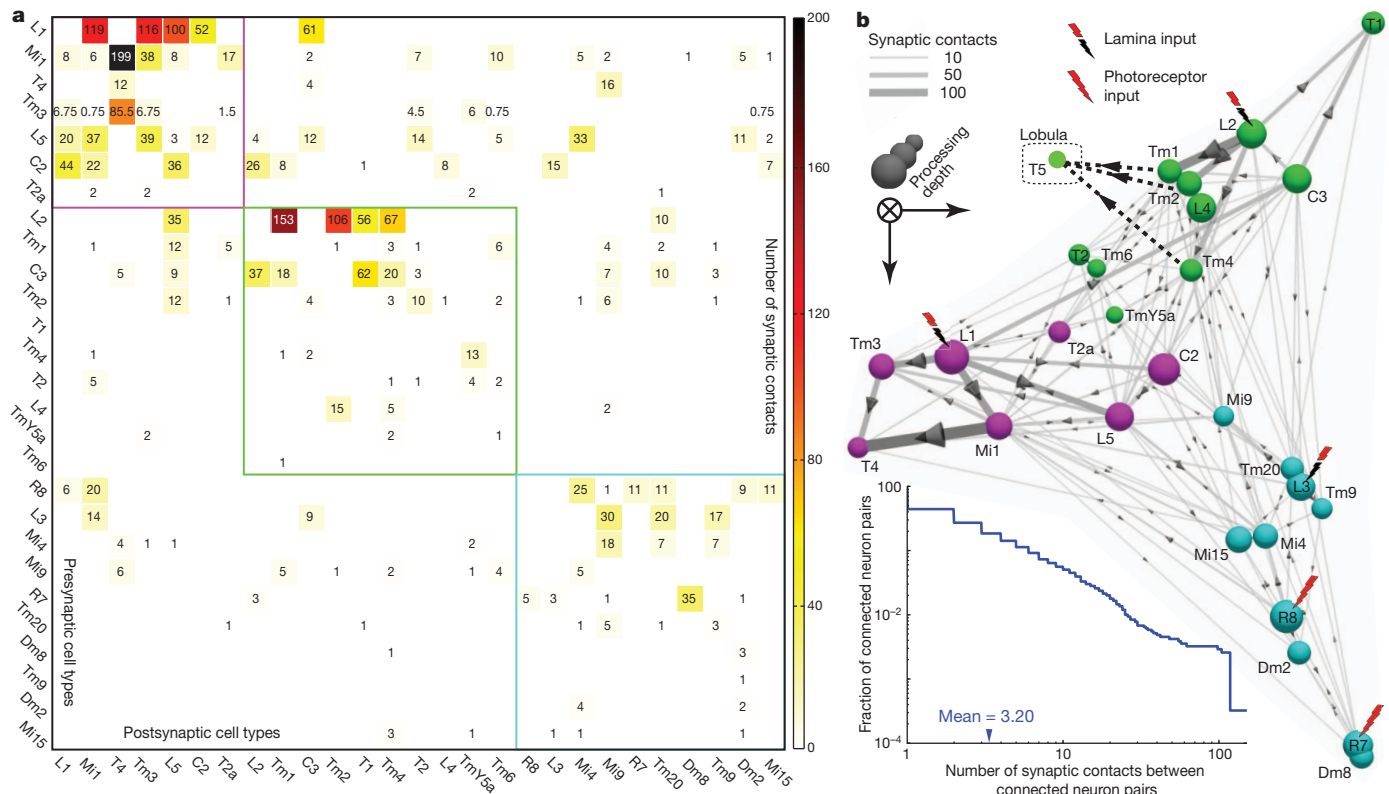


Figure 3 | Medulla connectome module. **a**, Synaptic connectivity matrix for modular cell types assembled from 2,495 synapses (Supplementary Table 1). Three pathways, identified via the Louvain clustering analysis⁴⁶, are labelled by coloured boxes. They are named by their primary input neuron(s): the L1 (magenta), L2 (green) and L3/R7/R8 (cyan) pathways. The pathways are ordered by the total number of connections within a pathway, in descending order, and the cell types, within each pathway, are ordered by the sum of their pre- and postsynaptic connections to and from other cell types within their

pathway, also in descending order. **b**, Medulla connectome module as a 3D graph. Cell types with stronger connections are positioned closer to each other, using the visualization of similarities layout algorithm⁴⁷. Three spatially segregated groups are observed that closely match the pathways identified through clustering (colouring of spheres). The dominant direction of signal flow is oriented into the page²². Inset in **b** shows the fraction of synaptic connections within the full connectome having a connection weight greater than indicated.

term ultraperiodic. We do not include infraperiodic tangential or local amacrine-like cells even if they have arborizations in every column because this cannot be determined unambiguously from our electron microscopy reconstruction (Supplementary Table 2). We used the existence of multiple representatives from adjacent columns within our electron microscopy reconstruction (Supplementary Fig. 1) to identify 25 cell types as synperiodic, as well as two cell types, Tm3 and T4, as ultraperiodic (with 1.5 and 4 cells per column, respectively) (Supplementary Table 2). We termed these 27 cell types modular.

Assuming that connections between modular cells are stereotypical between columns, we constructed the repeating circuit module by finding all connections between these cell types (Methods). Unlike sparse reconstructions, the resulting connectome module (Fig. 3a) accurately captures not only the presence but also the absence of strong connections between any two cell types.

To determine which neurons could be involved in different local computations, we dissected the connectome module into three separate signal processing pathways, using both a clustering and a layout algorithm (Fig. 3). We recognized them as the previously identified pathways, those of L1, L2 and L3/R7/R8. The downstream targets of R7 and R8 have previously been implicated in colour vision. Because colour pathways are separated into differing columns receiving inputs from either pale or yellow ommatidia²⁴, we expect that they should rely on infraperiodic cell types omitted from our connectome module. Therefore, the fine structure of the L3/R7/R8 pathway will be revisited elsewhere.

The remaining L1 and L2 pathways signal visual contrast, and are implicated in motion detection^{7,25–29}. Behavioural experiments and

electrophysiological recordings confirm this role for L1 and L2: not only is each necessary for aspects of motion detection^{29–31}, but, among the cells postsynaptic to the photoreceptors R1–R6, both are also mostly sufficient^{30,31} for the computation. However, L1 and L2 themselves lack directionally selective responses^{7,25}. Therefore, to search for motion detection circuit(s) within the connectome module, we examined the neurons downstream of L1 and L2 in more detail.

Candidate motion detection circuit

Several lines of evidence indicate that motion information computed downstream of L1 and L2 is relayed to the lobula plate via cell types T4 and T5 (ref. 25). First, recordings from LPTCs in fruitflies with genetically silenced T4 and T5 demonstrate that at least one of these columnar cell types is necessary to detect direction selectivity³². Second, T4 and T5 cells in *Drosophila* each comprise four subtypes differentiated by the lobula plate layer in which their axons arborize²⁰. Third, each of these four layers within the lobula plate exhibits activity in response to wide-field stimuli moving in a particular direction: downwards, upwards, backwards and forwards (Fig. 4b, e), revealed by their uptake of deoxyglucose^{11,27}. Finally, dendrites of LPTCs with different motion preference co-occupy the lobula plate layers corresponding to their directional preference²⁰ and, in addition, receive direct synaptic connections from T4 terminals²⁸. Collectively, these data suggest that each subtype of T4/T5 forms the output of motion detection circuits signalling a particular direction of motion.

Next, we argue that the direction-selective outputs of T5 and especially T4 are computed largely independently of each other. Consistent with stratum-overlap analysis in *Drosophila*²⁶ and large flies²⁵, our

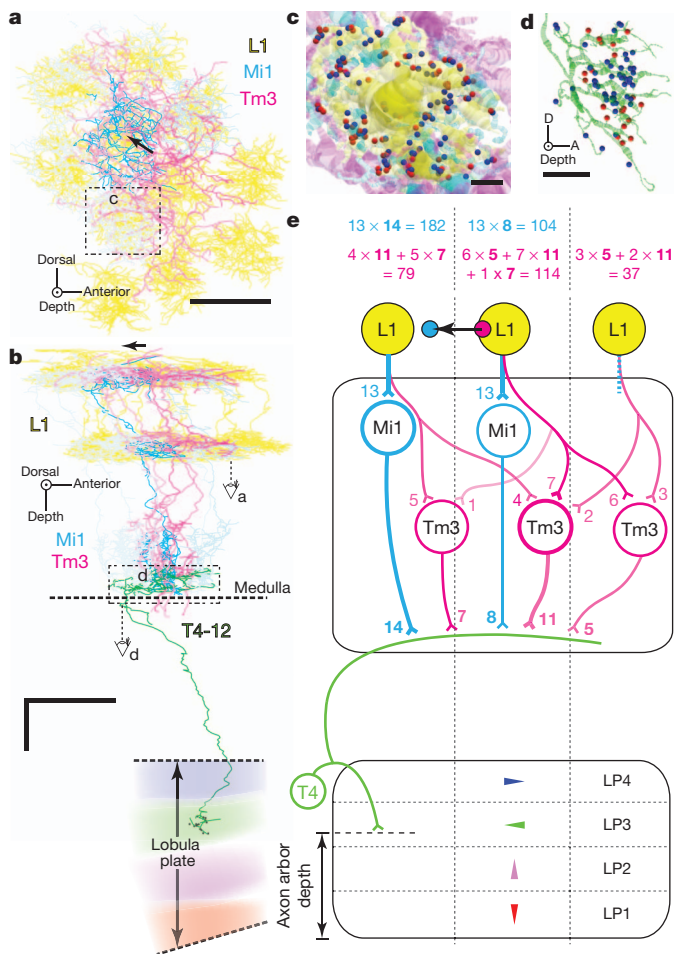


Figure 4 | Spatial displacement of Mi1- and Tm3-mediated inputs onto a single T4 cell (T4-12). **a**, Bottom view of dendrites of the Mi1 (cyan) and Tm3 (magenta) neurons presynaptic to T4-12, overlaid on the array of L1 axonal terminals (yellow). The colour saturation for each dendritic arbor reflects the number of synaptic contacts made onto T4-12 (see **b** and **d**). Arrow shows the displacement from the Tm3 centre of mass to the Mi1 centre of mass computed as illustrated in **e**. **b**, Side view of T4-12 and its presynaptic Mi1 and Tm3 cells. Direction preference for a T4 cell (coloured to match the directional preferences in **e**) is determined by the lobula plate arborization layer of the axon terminals (T-bars in black). **c**, Enlargement (dashed rectangle in **a**) showing reconstructed neurites of Mi1, Tm3 and L1 cells (without the weighted colours in **a**), and their synaptic contacts (L1 → Mi1: blue; L1 → Tm3: red). **d**, Reconstructed dendritic arbor of T4-12 with synapses from Mi1 (blue) and Tm3 (red). **e**, Cartoon of inputs to a single T4 cell through Mi1 and Tm3 cells. Mock synaptic weights illustrate how the receptive fields were computed. The centre of mass of Mi1 (or Tm3) component, blue (or red) circle, is computed by placing the mass corresponding to the compound synaptic weight from L1 through Mi1 (or Tm3) to T4 at the centre of the corresponding column. Scale bars, 8 μm (**a**), 8 μm (**b**), 1 μm (**c**) and 4 μm (**d**).

connectome (Fig. 3a, b) indicates that T4 belongs to the L1 pathway. Conversely, although we did not trace into the lobula, the dendrites of T5 cells co-occupy layers in the lobula with the axon terminals of neurons such as Tm1 (refs 20, 25), Tm2 (ref. 20) and Tm4 (ref. 20), which belong to the L2 pathway (Fig. 3b). Electrophysiological³⁰ and behavioural²⁹ evidence indicate that the L1 and L2 pathways in the connectome module (Fig. 3a, b) are computationally independent and correspond to ON and OFF pathways in the visual systems of vertebrates³⁰. Furthermore, most of the connections from the L2 to the L1 pathway arrive via L5 (Fig. 3a), a cell type not implicated in motion detection³³. Hence, we decided to search for a motion detection circuit downstream of L1 converging on T4 cells. This decision was made despite electrophysiological evidence showing a lack of direction

selectivity in T4 cells³⁴, but since the completion of our work, has been supported by calcium imaging of T4 cells³⁵.

To identify candidate elements of a motion detection circuit bridging between L1 and T4, we took advantage of the fact that motion detection is both fast and robust to noise^{16,17}, and consequently should be implemented by both feedforward and strong connections. Our dense electron microscopy reconstruction identified five cell types with significant input from L1: Mi1, Tm3, L5, C2 and C3 (Fig. 3a). Cell types Mi1 and Tm3 are the two largest recipients of L1 input, together accounting for more than half of the synaptic contacts of L1. In turn, Mi1 and Tm3 together contribute >80% of presynaptic inputs to T4 (including all inputs from both modular and non-modular cell types), thus forming the two strongest paths from L1 to T4. By contrast, cell type C3 contacts T4 with an order of magnitude fewer synapses than Mi1 and Tm3, suggesting that its contribution is far weaker. Finally, cell types L5 and C2 have no synapses directly with T4. These features lead us to suggest that Mi1 and Tm3 are the primary substrates for robust and fast motion detection within the L1 pathway.

Anatomical receptive fields of T4 cells

To explore further whether Mi1 and Tm3 cells converging on T4 cells could constitute the two arms of a correlation-based motion detector (Fig. 1a, b), we examined whether the motion axis defined by these inputs onto a particular T4 is consistent with its preferred direction, as measured by its outputs. This output-preferred direction was determined for 16 T4 neurons by tracing their axons into the lobula plate and identifying their arborization layer^{11,27} (Fig. 4b, e).

To compare the preference of T4 output with the motion axis arising from its inputs, we constructed the input motion axis by analysing the numbers of contacts from individual Mi1 and Tm3 cells onto the T4 neuron in question. We found that each T4 receives inputs from several Mi1 and Tm3 neurons suggesting that, unlike the circuits in Fig. 1a and b, several points in the visual field provide inputs into each arm of the motion detector (Fig. 4a, b, e). This observation is supported by the structure of sampling units inferred from recordings in blowfly H1 (ref. 36), which receives inputs from LPTCs³⁷. We therefore needed to characterize the inputs to each T4 as Mi1- and Tm3-mediated receptive field components, mapped into the visual field. To do this, we traced synaptic connections from L1 terminals in 19 columns (the reference column and surrounding 18 columns) to the downstream Mi1 and Tm3 cells and then from the Mi1 and Tm3 neurons onto T4 cells that receive input from the reference column (which also happen to number 19). The resulting receptive fields (Fig. 4a and Supplementary Fig. 4) show the T4 inputs mapped as if on the L1 array and hence into the visual field.

For all T4 cells, the Mi1- and Tm3-mediated components of the T4 receptive field overlap substantially with one another (Supplementary Fig. 4). Indeed, the centres of mass of the two components are displaced less than one inter-ommatidial distance (Fig. 5a). However, for 15 of the T4 cells, this displacement is still significantly greater ($P < 0.05$) than would have been obtained by chance from tracing errors. Such a small displacement magnitude relative to the widths of the receptive fields agrees with previous evidence inferred from blowfly H1 recordings and has been justified theoretically³⁶.

Is the direction of displacement between the Tm3 and Mi1 receptive-field components for a T4 neuron consistent with the directional preference of the neuron, as defined by the depth of its terminal axonal arborization in the lobula plate? Assuming that the direction of the displacement is determined from the Tm3 to Mi1 component centres of mass, Fig. 5b (top) shows that the direction of displacement agrees with the directional preference for three of the four lobula plate layers. The discrepancy in the direction of displacement and the front-to-back motion preference of T4 cells terminating in the fourth layer (lobula plate layer 4, LP4) may be caused by neglected circuits contributing specifically to the responses of these T4 neurons. For example, behavioural evidence implicates C3 neurons in front-to-back motion detection³³,

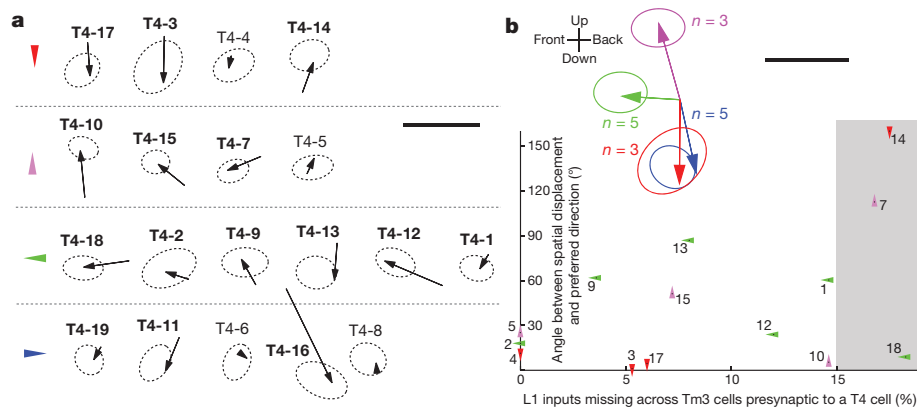


Figure 5 | Computed displacements for all T4 cells. **a**, Displacement vectors for each T4 neuron ($n = 19$). Neurons with significant displacement (names in bold) have 95% confidence intervals (ellipses) that exclude the origin (Methods). The vectors are in the ommatidial frame of reference (within $\sim 30^\circ$ of the visual axes). **b**, Top, mean displacement, computed from **a**, averaged over the cells with the same preferred direction of their output. Bottom, the angular difference between the spatial displacement for individual T4 neurons and the preferred direction of its output (for lobula plate layers 1–3 (LP1–3)) correlates with the fraction of missing L1 inputs (Methods). T4 cells with $>15\%$ of missing L1 inputs were omitted from the mean displacements (top). Scale bars, 0.5 (**a**) and 0.2 (**b**) of the centre-to-centre distance between adjacent facets.

and, indeed, preliminary tracing results indicate that, despite C3 cells providing an order of magnitude fewer inputs to T4 cells than Mi1 or Tm3 cells, C3 neurons target LP4 T4 cells preferentially.

Some of the discrepancy between the receptive field offset and the directional preference of individual T4 cells (Fig. 5a) innervating lobula plate layers 1–3 is probably caused by a systematic error in our reconstruction resulting from the finite size of the reconstructed region. Indeed, the discrepancy between the measured input displacement for a given T4 and its predicted direction preference correlates with the weighted fraction of missing L1 inputs onto Tm3 cells upstream of that T4 (Fig. 5b, bottom), supporting the view that the fields of peripheral T4 cells may not be fully reconstructed. In addition, some of the remaining variation in the offset orientation may also be real, given the observed 60° – 90° half-width of the tuning curves obtained through calcium imaging of individual T4 subtypes³⁵.

Our choice to measure displacement from Tm3 to Mi1 (and not in the reverse order) seems arbitrary without including information about delays and synaptic polarity (Fig. 1a, b). To estimate a possible conduction delay, we measured both the path length and the calibre of the main axon trunks that conduct signals along the Mi1 and Tm3 cells from L1 synapses to T4 synapses and found them to be similar, within 10% of each other. Moreover, using a range of electrotonic parameters measured in other fly neurons³⁸, the corresponding cable delays were still only on the order of one millisecond, an order of magnitude less than that required for motion detection²⁹. Furthermore, although some neurotransmitters have been identified for the cell types involved, we do not know their associated receptors and hence the resulting synaptic polarity.

In the absence of evidence for both relative delay and synapse polarity, we are free to choose the measurement direction from Tm3 to Mi1, which leads to spatial displacements consistent with the directional preference predicted by the depth of the T4 terminal in the lobula plate. Assuming that the Mi1 and Tm3 inputs to T4 are combined with the same sign, as in the Hassenstein–Reichardt elementary motion detector (EMD) model⁴ (Fig. 1a), we predict that the Tm3 arm of the motion detector should introduce a longer delay than the Mi1 arm. If, however, the inputs were combined with opposing signs, as in the Barlow–Levick-like EMD model⁶ (Fig. 1b), then our prediction would be the opposite. Regarding the mechanism of the delay, having the two arms of the circuit implemented by different cell types allows the possibility that the delay may be implemented biologically by means of metabotropic receptors, as reported in the vertebrate retina³⁹.

Exploring the reconstructed T4 cells, we identified a hitherto unrecognized feature of their medulla dendritic arbors (see, however, T4a,d in Fig. 14 of ref. 20, and N. J. Strausfeld, personal communication): the dendritic branches of each T4 neuron are oriented primarily in one direction (Fig. 6a and Methods). Moreover, the branch orientation of each T4, measured from the dendrite tips to their bases, clusters around one of four directions (Fig. 6b). These four directions, when mapped from the medulla coordinate frame onto the visual field (Fig. 6c), align with the output direction preference for each lobula plate layer (Fig. 6b). This observation allowed us to cross-validate the classification of each of the 16 T4 cells into direction preference subtypes (Fig. 6a, b and Supplementary Fig. 5). We then used this observation to infer a direction preference for the remaining three T4 cells, for which tracing into the lobula plate could not be completed (Fig. 6c).

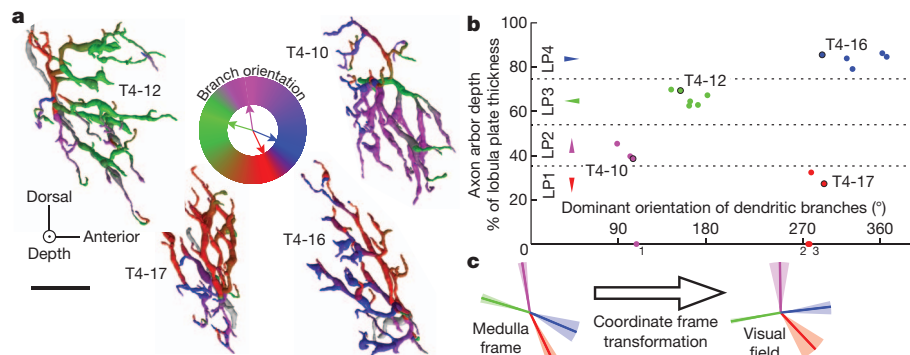


Figure 6 | Orientation of medulla dendritic arbors of T4 neurons correlates with axon terminal arborization layer in the lobula plate. **a**, Four representative medulla dendritic arbors of T4 cells. The colours represent local dendritic branch orientation. The colour map was constructed by assigning colours from each lobula plate layer (Fig. 4e) to the average dominant branch orientation over all neurons in each layer (arrows within colour map) and smoothly interpolating. **b**, Depth of axonal arbor of a T4 neuron within the lobula plate correlates with dominant dendritic branch orientation in the

medulla (Methods). In the depth axis, four layers are labelled and the neurons within each layer are coloured as in Fig. 4e. The dominant orientations of neurons with axons not traced to the lobula plate are plotted on the x axis (1: T4-5, 2: T4-4, 3: T4-14), and they are coloured with the colour of the cluster to which they most likely belong (Supplementary Fig. 5). **c**, Transforming the dominant dendritic orientation (\pm s.e.m.) from the space defined by the array of medulla columns (in layer M10) to the directions in visual space. Scale bar, 5 μ m.

Discussion

This report has introduced a new high-throughput, semi-automated pipeline for electron microscopy reconstruction, and applied it to reconstruct a connectome module comprehensively within the medulla, a neuropil that has long resisted such attempts. Furthermore, using connectomics, we identified M1 and Tm3 inputs to T4 neurons as the two arms of a candidate correlation-based motion detector. Although anatomy alone does not allow us to probe the nonlinear operation or the time delay, and hence distinguish between different correlation-based models^{5,6,40}, we were able to predict which cell type should introduce a longer delay, given their synaptic polarities (Fig. 1a, b).

Analogous to our proposed circuit downstream of L1, the connections within our electron microscopy reconstruction allow us to suggest candidate cell types—Tm1, Tm2 and Tm4—that may constitute the motion detection circuit downstream of L2. Confirmation of this suggestion must of course await dense reconstruction of the connections onto T5 neurons in the lobula.

This report has several interesting parallels with results from vertebrate retinæ. First, the existence of the four subtypes of T4 cells responding to the four cardinal directions of motion is reminiscent of the four subtypes of ON–OFF directionally selective ganglion cells (DSGCs) in the rabbit retina⁴¹. Second, our finding that directional selectivity of T4 cells is aligned with their dendritic orientation is reminiscent of JAM-B ganglion cells⁴² and starburst amacrine cells (SACs)⁴³ in the mouse retina. However, unlike JAM-B and SAC cells, the preferred direction of T4 cells is away from the tip of the dendrites and, unlike SAC cells but like JAM-B cells, all dendrites in one T4 point in the same direction. Third, the highly specific connections between SACs and DSGCs responsible for the directional selectivity of the latter were also demonstrated previously using large-scale connectomics⁴⁴. However, unlike the SAC-to-DSGC circuit, the circuit we report may compute directionally selective responses from non-directional inputs.

Our identification of the candidate motion detection pathway downstream of L1 was greatly aided by the comprehensiveness of our electron microscopy reconstruction. Relative to connections estimated by arbor overlap²⁶, having the precise synaptic counts allows us to unequivocally establish connections (Supplementary Fig. 6). In this way, we identified Tm3 as a primary component of the motion detection circuit, a fact that escaped previous researchers owing to its minimal arborization in M10. Furthermore, relative to sparse reconstructions in other systems, for example, synaptic connections between SACs and DSGCs⁴⁴, the comprehensiveness enables us to argue both the absence of alternative pathways and the numerical importance of the proposed pathway.

The significance of the dense medulla connectome also goes far beyond the local motion detector, applying to many other visual computations. Although much remains to be done, especially to incorporate tangential and infraperiodic cells fully, our connectome does contain the columnar neurons found in every column and hence removes a long-standing block to understanding insect vision. More generally, our results illustrate that, combined with a rich collection of experimental and theoretical results, connectomes can, by identifying underlying circuits, provide key insight into neuronal computation.

METHODS SUMMARY

A fly's brain was prepared for electron microscopy by high-pressure freezing/freezing substitution, followed by embedding, and sectioning. Sections were imaged using transmission electron microscopy. Electron micrographs were assembled into a three-dimensional stack correctly representing the relative locations of the imaged structures by means of nonlinear registration. The aligned stack of grayscale images was partitioned by machine learning algorithms into subsets of pixels, each belonging to only a single neuron (see <https://bitbucket.org/shivnaga/ssstem>). This over-segmented partition was manually inspected and agglomerated into individual neurons ('proofreading'). Presynaptic terminals and postsynaptic densities were then annotated by hand, and assigned to neurons (Supplementary Data 1). These manual steps required ~14,400 person-hours (including ~2,500 expert hours). The types of reconstructed neuron were determined by matching their shapes to examples from light microscopy. The full connectome was condensed

into a connectome module, which was partitioned into pathways using graph layout and clustering algorithms. By counting the numbers of synaptic contacts between L1, M1, Tm3 and T4 cells, we computed the relative displacement of the input components. We cross-validated this displacement against the direction preference of T4 cells found by tracing their axons into the lobula plate.

Full Methods and any associated references are available in the online version of the paper.

Received 8 March; accepted 12 July 2013.

- Heisenberg, M. & Wolf, R. *Vision in Drosophila. Genetics of Microbehaviour* (Springer Verlag, 1984).
- Laughlin, S. B. Matching coding, circuits, cells, and molecules to signals: General principles of retinal design in the fly's eye. *Prog. Retin. Eye Res.* **13**, 165–196 (1994).
- Strausfeld, N. J. & Nüssel, D. R. in *Handbook of Sensory Physiology* (eds Autrum, H. et al.) 1–132 (Springer-Verlag, 1981).
- Hassenstein, B. & Reichardt, W. Systemtheoretische Analyse der Zeit-, Reihenfolgen- und Vorzeichenbewertung bei der Bewegungsperzeption des Rüsselkäfers *Chlorophanus*. *Z. Naturforsch. B* **11**, 513–524 (1956).
- Reichardt, W. in *Sensory Communication* (ed. Rosenblith, W. A.) 303–317 (MIT Press, 1961).
- Barlow, H. B. & Levick, W. R. The mechanism of directionally selective units in rabbit's retina. *J. Physiol. (Lond.)* **178**, 477–504 (1965).
- Borst, A., Haag, J. & Reiff, D. F. Fly motion vision. *Annu. Rev. Neurosci.* **33**, 49–70 (2010).
- Rivera-Alba, M. et al. Wiring economy and volume exclusion determine neuronal placement in the *Drosophila* brain. *Curr. Biol.* **21**, 2000–2005 (2011).
- Meinertzhagen, I. A. & Sorra, K. E. Synaptic organization in the fly's optic lamina: few cells, many synapses and divergent microcircuits. *Prog. Brain Res.* **131**, 53–69 (2001).
- Takemura, S. Y., Lu, Z. & Meinertzhagen, I. A. Synaptic circuits of the *Drosophila* optic lobe: the input terminals to the medulla. *J. Comp. Neurol.* **509**, 493–513 (2008).
- Buchner, E., Buchner, S. & Bülthoff, I. Deoxyglucose mapping of nervous activity induced in *Drosophila* brain by visual movement. *J. Comp. Physiol. A* **155**, 471–483 (1984).
- Krapp, H. G. & Hengstenberg, R. Estimation of self-motion by optic flow processing in single visual interneurons. *Nature* **384**, 463–466 (1996).
- Joesch, M., Plett, J., Borst, A. & Reiff, D. F. Response properties of motion-sensitive visual interneurons in the lobula plate of *Drosophila melanogaster*. *Curr. Biol.* **18**, 368–374 (2008).
- White, J. G., Southgate, E., Thomson, J. N. & Brenner, S. The structure of the nervous system of the nematode *Caenorhabditis elegans*. *Phil. Trans. R. Soc. Lond. B* **314**, 1–340 (1986).
- Kirschfeld, K. in *Information Processing in the Visual System of Arthropods* (ed. Wehner, R.) 61–74 (Springer Verlag, 1972).
- Riehle, A. & Franceschini, N. Motion detection in flies: parametric control over ON–OFF pathways. *Exp. Brain Res.* **54**, 390–394 (1984).
- Schilling, F. H., Mastebroek, H. A. K., Bult, R. & Lenting, B. P. M. Properties of elementary movement detectors in the fly *Calliphora erythrocephala*. *J. Comp. Physiol. A* **165**, 179–192 (1989).
- Helmstaedter, M., Briggman, K. L. & Denk, W. 3D structural imaging of the brain with photons and electrons. *Curr. Opin. Neurobiol.* **18**, 633–641 (2008).
- Chklovskii, D. B., Vitaladevuni, S. & Scheffer, L. K. Semi-automated reconstruction of neural circuits using electron microscopy. *Curr. Opin. Neurobiol.* **20**, 667–675 (2010).
- Fischbach, K.-F. & Dittrich, A. P. M. The optic lobe of *Drosophila melanogaster*. I. A Golgi analysis of wild-type structure. *Cell Tissue Res.* **258**, 441–475 (1989).
- Song, S., Sjöström, P. J., Reigl, M., Nelson, S. & Chklovskii, D. B. Highly nonrandom features of synaptic connectivity in local cortical circuits. *PLoS Biol.* **3**, e68 (2005).
- Varshney, L. R., Chen, B. L., Paniagua, E., Hall, D. H. & Chklovskii, D. B. Structural properties of the *Caenorhabditis elegans* neuronal network. *PLOS Comput. Biol.* **7**, e1001066 (2011).
- Campos-Ortega, J. A. & Strausfeld, N. J. in *Information Processing in the Visual Systems of Arthropods* (ed. Wehner, R.) 31–36 (Springer Verlag, 1972).
- Franceschini, N., Kirschfeld, K. & Minke, B. Fluorescence of photoreceptor cells observed *in vivo*. *Science* **213**, 1264–1267 (1981).
- Douglass, J. K. & Strausfeld, N. J. Anatomical organization of retinotopic motion-sensitive pathways in the optic lobes of flies. *Microsc. Res. Tech.* **62**, 132–150 (2003).
- Bausenwein, B., Dittrich, A. P. & Fischbach, K. F. The optic lobe of *Drosophila melanogaster*. II. Sorting of retinotopic pathways in the medulla. *Cell Tissue Res.* **267**, 17–28 (1992).
- Bausenwein, B. & Fischbach, K. F. Activity labeling patterns in the medulla of *Drosophila melanogaster* caused by motion stimuli. *Cell Tissue Res.* **270**, 25–35 (1992).
- Strausfeld, N. J. & Lee, J. K. Neuronal basis for parallel visual processing in the fly. *Vis. Neurosci.* **7**, 13–33 (1991).
- Clark, D. A., Bursztyn, L., Horowitz, M. A., Schnitzer, M. J. & Clandinin, T. R. Defining the computational structure of the motion detector in *Drosophila*. *Neuron* **70**, 1165–1177 (2011).
- Joesch, M., Schnell, B., Raghu, S. V., Reiff, D. F. & Borst, A. ON and OFF pathways in *Drosophila* motion vision. *Nature* **468**, 300–304 (2010).
- Rister, J. et al. Dissection of the peripheral motion channel in the visual system of *Drosophila melanogaster*. *Neuron* **56**, 155–170 (2007).

32. Schnell, B., Raghu, S. V., Nern, A. & Borst, A. Columnar cells necessary for motion responses of wide-field visual interneurons in *Drosophila*. *J. Comp. Physiol. A* **198**, 389–395 (2012).
33. Tuthill, J. C., Nern, A., Rubin, G. M. & Reiser, M. B. Contributions of the 12 neuron classes in the fly lamina to motion vision. *Neuron* **79**, 128–140 (2013).
34. Douglass, J. K. & Strausfeld, N. J. Visual motion-detection circuits in flies: parallel direction-and non-direction-sensitive pathways between the medulla and lobula plate. *J. Neurosci.* **16**, 4551–4562 (1996).
35. Maisak, M. S. *et al.* A directional tuning map of *Drosophila* elementary motion detectors. *Nature* <http://dx.doi.org/10.1038/nature12320> (this issue).
36. Srinivasan, M. & Dvorak, D. Spatial processing of visual information in the movement-detecting pathway of the fly. *J. Comp. Physiol. A* **140**, 1–23 (1980).
37. Haag, J. & Borst, A. Recurrent network interactions underlying flow-field selectivity of visual interneurons. *J. Neurosci.* **21**, 5685–5692 (2001).
38. Gouwens, N. W. & Wilson, R. I. Signal propagation in *Drosophila* central neurons. *J. Neurosci.* **29**, 6239–6249 (2009).
39. Ashmore, J. F. & Copenhagen, D. R. Different postsynaptic events in two types of retinal bipolar cell. *Nature* **288**, 84–86 (1980).
40. Mizunami, M. Synaptic rectification model equivalent to the correlation-type movement detector. *Biol. Cybern.* **64**, 1–6 (1990).
41. Oyster, C. W. & Barlow, H. B. Direction-selective units in rabbit retina: distribution of preferred directions. *Science* **155**, 841–842 (1967).
42. Kim, I.-J., Zhang, Y., Yamagata, M., Meister, M. & Sanes, J. R. Molecular identification of a retinal cell type that responds to upward motion. *Nature* **452**, 478–482 (2008).
43. Euler, T., Detwiler, P. B. & Denk, W. Directionally selective calcium signals in dendrites of starburst amacrine cells. *Nature* **418**, 845–852 (2002).
44. Briggman, K. L., Helmstaedter, M. & Denk, W. Wiring specificity in the direction-selectivity circuit of the retina. *Nature* **471**, 183–188 (2011).
45. Meinertzhagen, I. & Hanson, T. in *The Development of Drosophila Melanogaster* Vol. 2 (eds Bate, M. & Martinez Arias, A.) 1363–1491 (Cold Spring Harbor Laboratory Press, 1993).
46. Blondel, V. D., Guillaume, J. L., Lambiotte, R. & Lefebvre, E. Fast unfolding of communities in large networks. *J. Stat. Mech.* **2008**, P10008 (2008).
47. Eck, N. & Waltman, L. VOS: a new method for visualizing similarities between objects. *Adv. Data Anal.* 299–306 (2007).

Supplementary Information is available in the online version of the paper.

Acknowledgements We acknowledge the technical support of all members of the Janelia FlyEM project and the Chklovskii group, past and present. We thank S. Laughlin for numerous discussions, and M. Reiser and N. Verma for commenting on the manuscript. We thank A. Borst, C. Desplan, C.-H. Lee, T. Clandinin and L. Zipursky for discussions and granting us access to their data before publication.

Author Contributions D.B.C. and I.A.M. designed the research. Z.L., Sh.T. and R.D.F. prepared and imaged the sample. D.J.O., P.W., S.M.P., S.V. and W.T.K., under the guidance of D.B.C. and L.K.S., developed software for the reconstruction. Sh.T. annotated the micrographs, proofread the segmentation, and assembled the connectome, with the help of other proofreaders (Sa.T. K.B., L.-A.C., O.O., M.A.S., V.S. and C.S.), supervised by P.K.R. and J.A.H. A.N. and G.M.R. provided and A.N. analysed light microscopy images. L.K.S. and A.B. performed data analysis and T.Z. aided in visualization. A.B. and D.B.C. studied the motion detection circuit. A.B., D.B.C., I.A.M. and L.K.S. wrote the paper, with contributions from Sh.T. and A.N.

Author Information Reprints and permissions information is available at www.nature.com/reprints. The authors declare no competing financial interests. Readers are welcome to comment on the online version of the paper. Correspondence and requests for materials should be addressed to D.B.C. (mitya@janelia.hhmi.org) or I.A.M. (iam@dal.ca).

METHODS

Tissue preparation, electron microscopy and imaging. The right part of the brain of a wild-type Oregon R female fly was serially sectioned into 40-nm slices. A total of 1,769 sections, traversing the medulla and downstream neuropils (Fig. 1c), were imaged at a magnification of $\times 5,000$. This process is detailed in the Supplementary Methods.

Semi-automated reconstruction pipeline. To obtain a dense electron microscopy reconstruction of the reference column, we used a sequence of automated alignment and segmentation steps, followed by manual proofreading and reconstruction, which we described as the semi-automated reconstruction pipeline¹⁹.

Image alignment. We first found a rough alignment of the full image stack, ignoring artefacts such as folds, tears and dirt occlusions, by using TrakEM2 rigid registration⁴⁸ to align image blocks consisting of 20 sections of 9×9 mosaics, and then aligning blocks by an automated search over images at the centre of each mosaic. This rough alignment served to determine which images overlapped, allowing more precise analysis of tissues with artefacts, and in particular, large folds. Pixels much darker than average were assumed to correspond to folds and were used to divide each image into two or more connected components, called patches. For each pair of overlapping patches, both within a section (along the boundary) and section-to-section, points of correspondence were found by correlation (~ 1 per 500,000 overlapping pixels). A least-squares fit of these points with regularization for scale and skew was then used to produce a global affine alignment of all patches. Examination of errors from this fit identified images for which the automatic division into patches was inaccurate, and these divisions were corrected manually. Once a satisfactory fit was obtained, each patch of each image was then slightly distorted to provide a best match to its neighbour(s) while still remaining close to the global affine. More details are available in the ref. 49.

Automatic image segmentation. In the next step, we partitioned the medulla region of interest within the aligned stack of greyscale images into subsets of pixels belonging to individual neurons. Given that the resolution of the transmission electron microscopy (TEM) data set is anisotropic, we developed a two-step process comprising 2D segmentation to identify cross-sections of neurons followed by linkage of these segments in 3D. No single algorithm was used on all data, because many different segmentation techniques were tried in parallel with proofreading efforts, and it was counter-productive to re-segment portions already corrected. A typical 2D segmentation step entailed creating boundary probability maps using morphological features^{50–52} followed by boosted edge learning⁵³, mitochondria detection to reduce false boundaries⁵⁴, followed by watershed segmentation⁵⁵ and agglomerative clustering⁵⁶ using mean and median boundary values to create 2D segments. The 3D linkage step constructed a linkage graph of consecutive 2D segments in adjacent sections. Again, several techniques were used, including simple metrics such as overlap, and machine-learning approaches that computed appropriate weights of features from previously proofread data. Further details of some of our automatic segmentation approaches can be found in previous publications^{19,57}. Given that all segmentation algorithms make mistakes resulting from imaging artefacts and low z -resolution, and because manual correction of over-segmentations is easier than under-segmentations, we tuned our automatic algorithms to produce an over-segmented image volume. Furthermore, we preserved watershed regions called super-pixels to facilitate the manual correction of over-segmentation in the next step. We have released the latest (and we believe best) version of the segmentation code that we used (<https://bitbucket.org/shivnaga/sstem>), but caution the reader that even our best automatic segmentation required extensive manual proofreading, correction, and annotation (see below) to yield the results we report in this paper.

Proofreading and reconstruction. We next inspected the results of automatic segmentation, corrected remaining errors, and assigned synapses to the proofread cell arbors. Because this was time-consuming, we trained a group of professional editors, referred to as proofreaders, whose work was supervised by three experienced electron microscopists (Sh.T., Sa.T. and P.K.R.) (experts). Proofreaders and experts performed their tasks using a dedicated custom software tool, Raveler (D.J.O. *et al.*, manuscript in preparation). In total, these proofreading steps took $\sim 12,940$ person-hours (including 900 person-hours contributed by our experts). There were five key steps within the reconstruction procedure: (1) volume proofreading, (2) synapse annotation, (3) postsynaptic tracing, (4) anchor body refinement, and (5) selective sparse tracing, detailed in the Supplementary Methods.

Reliability of the wiring diagram. As introduced above, we assigned two proofreaders to each synapse, to increase the reliability of proofreading. Characterizing this, in 48.2% of cases both proofreaders were unable to identify a parent cell either because they could not trace the process confidently or because it left the medulla region of interest. In 44.0% of cases, both proofreaders traced the PSD to the same anchor body, and in 7.5% of cases one proofreader was unable to complete the tracing whereas the other traced the PSD to an anchor body (numbers extracted from Supplementary Table 1). However, only in very few cases

(0.23%) did the two proofreaders reach different anchor bodies. These numbers suggest that a large fraction of connections will be missed, following the two proofreader agreement process; however, all connections that are identified have a very high probability of being correct.

To assess our reconstruction quality further, we generated two connectomes from the dual proofreader results—an inclusive version that included connections found by either proofreader, and a consensus version in which connections were accepted only when both proofreaders agreed. Comparing these two connectomes was generally reassuring. Although the inclusive connectome has $\sim 16\%$ more connections, all the additional connections had only one synaptic contact. All connections with two or more synapses are present in both connectomes (Supplementary Table 1). We used the consensus connectome for all our analyses. However, the conclusions remain unchanged when using the inclusive connectome.

In general, the high rates of missed synaptic contacts in our proofreading was tolerable for our project because our intent was to study connections with several, parallel synaptic contacts. We could confirm that the connectome contains a large fraction of such strong connections by plotting the distribution of the number of contacts between connected pairs of cells.

We found a strongly heavy-tailed distribution of the total numbers of contacts for each connected pair both in the whole connectome (inset in Fig. 3b), and within the subset of sparsely-traced cell-types involved in motion detection (Supplementary Fig. 3). Given that the sizes of T-bars within the medulla are relatively uniform (A. McGregor *et al.*, unpublished observations) and the size of synaptic structures is thought to correlate with their physiological strength⁵⁸, we viewed the number of parallel synaptic contacts between two neurons as a proxy of synaptic weight. Furthermore, making an assumption that the probability of missing a synaptic contact during proofreading is uniform across all postsynaptic sites, we can estimate that the consensus connectome contains all connections with >5 synapses with a confidence level $>95\%$ (Supplementary Methods). Therefore, we believe our consensus connectome is both precise and comprehensive for strong connections.

Constructing a connectome module. In constructing a repeating module within the medulla connectome, all the members of each class of neurons within the reference column were identified, and the number of synapses from those neurons to all other neurons of the postsynaptic class was averaged over the pre-synaptic cells. For the ultraperiodic cell types, for example, Tm3, this could result in a fractional weight. Furthermore, because there are 1.5 Tm3 cells per column on average, we computed the synaptic weight by multiplying it by 1.5. These fractional weights provide the mean connection strength over different columns, because some columns have only a single Tm3, whereas others have two.

The directional summation that was used here was chosen because, in our reconstruction, we attempted to proofread each postsynaptic element to its associated neuron. However, we did not attempt to proofread every presynaptic site back to its parent neuron (as some such elements might derive from non-reference columns, which were not densely reconstructed).

This method was modified for the four connections in the motion detection circuit: L1 to Mi1, L1 to Tm3, Mi1 to T4, and Tm3 to T4. In these cases, the number of synaptic contacts from the densely reconstructed medulla connectome was replaced by the number of synaptic contacts identified during sparse tracing of these specific connections (Supplementary Table 3).

Computing the Mi1 and Tm3 receptive field components. We computed the Mi1 and Tm3 components of the receptive field for each T4, by multiplying the number of synaptic contacts from each L1 neuron to a single intermediate Mi1 or Tm3 neuron by the number of contacts from that intermediate cell to the T4, and then summing over all the Mi1 and Tm3 neurons that receive input from the same L1 (Fig. 4e). This multiplication is equivalent to counting the number of independent synaptic routes from each L1 to each T4, in which each route must use a different pair of the synaptic contacts between the L1 and the intermediate target cells, and the intermediate targets and the T4.

Monte Carlo error estimate. Our proofreading methodology results in very few false positive errors, but many false negative errors between neuron pairs (see earlier). Therefore, it is highly probable that the observed number of synaptic contacts (m) is a subset of a higher, true number of synaptic contacts between two neurons (n). Assuming that, for any connected pair of neurons each synaptic contact had an equal false negative probability, and using that probability in a binomial distribution, our goal was to estimate the posterior probability, $P(n|m)$ (that is, the probability of the true n given the observed m), for different values of n . To do this, because the previous distribution over n is unknown, we approximated this posterior probability by the likelihood, $P(m|n)$ (that is, probability of observing m given some value of the true n), for different values of n . We generated 1,000 different estimates of the true connection weight, for every connected neuron pair, by sampling from the set of possible n values with the computed

likelihood given each value of n . Neuron pairs that were disconnected because of high false negative error rates were also allowed to connect if their neurite profiles overlapped in 3D. The number of contacts was estimated using the same sampling method as before (but with m equal to zero). In this way, we generated 1,000 different connectivity matrices. The displacement was then computed for each matrix. The eigenvalues and eigenvectors of the covariance matrix over all displacement vectors were computed, and used to plot an ellipse along the eigenvector axes with 2σ confidence intervals (Fig. 5a). To extend this construction to the mean displacement over a group of neurons, 1,000 variations of the mean were computed, by first sampling from the displacements generated for each neuron, and then computing the mean for each set of samples. The ellipses were then computed, in the same way as before, over this set of 1,000 mean values (Fig. 5b, top).

Effect of limited reconstruction size. Because the spread of the dendritic arbors of the Tm3 cells connected to a given T4 is greater than that of the Mi1 cells, Tm3 cells are more likely to be partially reconstructed, and, hence, missing L1 inputs near the edges of our 19 column reconstruction. To provide a measure of the effect of this cut-off on each T4, we first visually inspected each Tm3 neuron, and classified it into one of four classes, depending on the percentage of the arbor that was missing from the 19 column reconstruction. Tm3 cells that were reconstructed fully received input from an average of six L1 neurons. In contrast, Tm3 cells in the fourth class, which had most of their arbor outside our region of interest, received input from an average of only two L1 neurons. By summing up the fraction of L1 inputs missing, weighted by the fraction of inputs provided by each Tm3 class to the given T4, we obtained an estimate of the weighted fraction of L1 inputs missing (through the Tm3 channel) for each T4 (the x axis in Fig. 5b, bottom). We also used this metric to justify the removal of T4 cells missing >15% of their weighted L1 inputs (through the Tm3 channel), in constructing the mean responses for T4 cells with the same output direction preferences (Fig. 5b, top).

Dendrite orientation. After proofreading, the T4 arborizations within M10 were skeletonized, starting from the centre of the thickest branch, adapting the method of ref. 59 with a modified weighting function. The axonal branch point was determined by Sh.T. so as to identify the dendritic part of the medulla arborization precisely. The local orientation around each dendritic node was computed (using three nodes in both directions around each node, and ignoring any nodes with fewer than three adjacent nodes in both directions). The dominant dendritic branch orientation, for each T4 (Fig. 6b), was computed by taking the fast fourier transform (MATLAB and Statistics Toolbox, version R2012b) of the distribution of orientations across nodes, and defined to be the phase of the fundamental mode component of the transformation. Assuming a normal distribution for the dominant orientation of the cells assigned to a layer (via their axon arbor depth),

we computed the probability of each untraced T4 lying within each cluster of cells, given its measured dominant orientation. The assignment of cell T4-4 to layer 1 was significant ($P < 0.05$), but the assignment of the other two cells was not. The colour map for the dendritic arbors (Fig. 6a and Supplementary Fig. 5) was chosen by centring colours on the average of the dendritic branch orientation for each cluster (Fig. 6b), and varying the colour continuously between clusters.

Data access. At publication the skeletons of all cells will be uploaded to <http://neuromorpho.org>. We will host a website (<https://openwiki.janelia.org/wiki/display/flyem/Medulla+TEM+Reconstruction>) that will allow the viewer to search the consensus connectome for connected neuron pairs. We will also provide the entire segmentation with synapse annotations, along with Raveler to open the data set, upon request. The requesting party will need to supply a hard drive.

48. Cardona, A. *et al.* TrakEM2 software for neural circuit reconstruction. *PLoS ONE* **7**, e38011 (2012).
49. Scheffer, L., Karsh, B. & Vitaladevuni, S. Automated alignment of imperfect EM images for neural reconstruction. Preprint at <http://arXiv.org/abs/1304.6034> (2013).
50. Canny, J. A computational approach to edge detection. *IEEE Trans. Pattern Anal. Mach. Intell.* **PAMI-8**, 679–698 (1986).
51. Martin, D. R., Fowlkes, C. C. & Malik, J. Learning to detect natural image boundaries using local brightness, color, and texture cues. *IEEE Trans. Pattern Anal. Mach. Intell.* **26**, 530–549 (2004).
52. Soille, P. *Morphological Image Analysis: Principles and Applications* 2nd edn, 316 (Springer-Verlag New York, 2003).
53. Dollar, P., Tu, Z. & Belongie, S. Supervised learning of edges and object boundaries. *IEEE Comp. Soc. Conf. Comp. Vis. Pattern Rec.* **2**, 1964–1971 (2006).
54. Vitaladevuni, S., Mishchenko, Y., Genkin, A., Chklovskii, D. C. & Harris, K. M. Mitochondria detection in electron microscopy images. *Workshop Microscopic Image Anal. Appl. Biol.* <http://www.miaab.org/miaab-2008-papers/21-miaab-2008-abstract-05.pdf> (2008).
55. Vincent, L. & Soille, P. Watersheds in digital spaces: an efficient algorithm based on immersion simulations. *IEEE Trans. Pattern Anal. Mach. Intell.* **13**, 583–598 (1991).
56. Mohanta, P. P., Mukherjee, D. P. & Acton, S. T. Agglomerative clustering for image segmentation. *Int. Conf. Pattern Rec.* **1**, 664–667 (2002).
57. Vitaladevuni, S. N. & Basri, R. Co-clustering of image segments using convex optimization applied to EM neuronal reconstruction. *IEEE Comp. Soc. Conf. Comp. Vis. Pattern Rec.* <http://dx.doi.org/10.1109/CVPR.2010.5539901> 2203–2210 (2010).
58. Kasai, H., Matsuzaki, M., Noguchi, J., Yasumatsu, N. & Nakahara, H. Structure–stability–function relationships of dendritic spines. *Trends Neurosci.* **26**, 360–368 (2003).
59. Sato, M., Bitter, I., Bender, M. A., Kaufman, A. E. & Nakajima, M. TEASAR: Tree-structure extraction algorithm for accurate and robust skeletons. *Eighth Pac. Conf. Comp. Graphics Appl.* <http://dx.doi.org/10.1109/PCCGA.2000.883951> 281–287, 449 (2000).